The Relative Importance of Updraft and Cold Pool Characteristics in Supercell Tornadogenesis Using Highly Idealized Simulations

JANNICK FISCHER[a] AND JOHANNES M. L. DAHL[a]

[a] *Department of Geosciences, Texas Tech University, Lubbock, Texas*

(Manuscript received 27 April 2020, in final form 11 September 2020)

ABSTRACT: In the recent literature, the conception has emerged that supercell tornado potential may mostly depend on the strength of the low-level updraft, with more than sufficient subtornadic vertical vorticity being assumed to be present in the outflow. In this study, we use highly idealized simulations with heat sinks and sources to conduct controlled experiments, changing the cold pool or low-level updraft character independently. Multiple, time-dependent heat sinks are employed to produce a realistic near-ground cold pool structure. It is shown that both the cold pool and updraft strength actively contribute to the tornado potential. Furthermore, there is a sharp transition between tornadic and nontornadic cases, indicating a bifurcation between these two regimes triggered by small changes in the heat source or sink magnitude. Moreover, larger updraft strength, updraft width, and cold pool deficit do not necessarily result in a stronger maximum near-ground vertical vorticity. However, a stronger updraft or cold pool can both drastically reduce the time it takes for the first vortex to form.

KEYWORDS: Tornadogenesis; Updrafts/downdrafts; Supercells; Large eddy simulations

1. Introduction

Supercell tornadogenesis relies on the interaction of two processes: internally produced near-ground vertical vorticity and the strong upward accelerations below the mesocyclone (Davies-Jones 2015). Regarding the first aspect, over the past decades many studies have been performed to find the main source of near-ground vertical vorticity for tornadoes. It has been largely accepted that the initial vertical vorticity arises from the Davies-Jones and Brooks (1993, hereafter DJB93) mechanism, which includes baroclinic horizontal vorticity production and tilting into the vertical by downdraft gradients (e.g., Rotunno and Klemp 1985; Walko 1993; Dahl et al. 2014; Parker and Dahl 2015). More recently, surface friction has been demonstrated to be a viable source of horizontal vorticity for tornadoes, which may be tilted upward at the base of existing tornadoes or lead to early tornadogenesis before a cold pool has been established (Schenkman et al. 2014; Roberts et al. 2016, 2020; Boyer and Dahl 2020). However, some recent studies have focused on the second process, the intensification of the low-level[1] updraft by an upward-directed vertical perturbation pressure gradient force (VPPGF). This force tends to be dominated by the nonlinear dynamic VPPGF (Markowski and Richardson 2014), which is proportional to the strength of the mesocyclone via ζ^2, where ζ is vertical vorticity, which results from upward tilting of ambient horizontal vorticity (Rotunno 1981; Davies-Jones 1984; Dahl 2017). Therefore, varying the horizontal vorticity in the environment leads to different degrees of low-level upward accelerations and greatly influences tornado potential (Markowski and Richardson 2014; Coffer and Parker 2015, 2017, 2018). Furthermore, in recent simulations the streamwise vorticity current (SVC) has been implicated as modulating the low-level updraft intensification as well (Orf et al. 2017; see also Rotunno and Klemp 1985). Based on these studies, Coffer and Parker (2018) suggested that "all surface-based supercells possess ample subtornadic surface vertical vorticity" and that in fact a strong and steady low-level updraft might be the most important factor for tornadogenesis.

This theory is supported by the fact that environmental parameters that serve as proxies for a strong low-level updraft, including 0–3 km convective available potential energy (CAPE) and 0–1 km storm-relative helicity (SRH), can detect environments with potential for strong tornadoes quite well (Rasmussen and Blanchard 1998; Thompson et al. 2003; Markowski et al. 2003; Craven and Brooks 2004; Sherburn et al. 2016). In their most recent work, Coffer et al. (2019) showed that using SRH over an even shallower layer (0–500 m) in their implementation of the significant tornado parameter (STP) improved the forecast skill. This result is closely related to other studies highlighting the importance of the hodograph shape in the lowest kilometer and the associated streamwise horizontal vorticity component, which can favor a more intense and robust low-level updraft (Thompson and Edwards 2000; Esterheld and Giuliano 2008; Parker 2014; Coffer and Parker 2017; Coffer et al. 2017; Coffer and Parker 2018). On the other hand, even in favorable environments only the minority of supercells are tornadic, leading to high false alarm ratios of warnings issued by the

[1] We will use the term "low level" for heights between 0.5 and 1.5 km above ground level (AGL).

Supplemental information related to this paper is available at the Journals Online website: https://doi.org/10.1175/JAS-D-20-0126.s1.

Corresponding author: Jannick Fischer, jannick.fischer@ttu.edu

Publisher's Note: This article was revised on 25 November 2020 to correct the Coffer and Parker (2016) reference to Coffer and Parker (2017).

DOI: 10.1175/JAS-D-20-0126.1

National Weather Service and raising the question of what makes tornadic supercells so special as compared to nontornadic cells in the same environment (Anderson-Frey et al. 2016).

These differences between similar storms are difficult to investigate. Observational studies often focus on one case and cannot be directly compared among each other. In addition, especially the key features for tornadogenesis (updraft and cold pool processes) are not easy to measure. Even idealized thunderstorm simulations based on realistic base states, which we will refer to as full-physics simulations, have disadvantages when only looking at the tornadogenesis process. First, they are not efficient because computationally expensive numerical simulations have to be performed with a high resolution over several hours and on a large domain to allow the storms to develop. Even if a tornado is successfully produced, only a relatively small area and time period will be analyzed. Second, controlled experiments can hardly be designed as the low-level updraft and cold pool character depend on the dynamics of the storm (i.e., time-dependent interactions of the updraft, hydrometeor production, downdrafts, and the near-storm environment).

For these reasons, this study adopts a different, highly idealized simulation approach based on the work of Markowski and Richardson (2014, hereafter MR14), also known as pseudostorm or "toy model." Instead of triggering storms in an unstable model environment, in MR14 the authors imitated the latent heat exchange of a storm by adding terms to CM1's potential temperature tendency equation. A cylindrical heat source was used to simulate the supercell updraft while a heat sink reproduced the storm-scale downdraft and cold pool. This simple setup was sufficient to successfully reproduce many of the typical supercell structures. In addition to the importance of the low-level shear for updraft intensification, they found tornadogenesis failure mainly being connected to the strength of the heat sink. With a very strong heat sink, the outflow tended to undercut the updraft while too weak a heat sink resulted in the cyclonic vertical-vorticity maximum remaining upstream of the updraft.

In this study we modify MR14's method to directly simulate only the low-level supercell-like updraft (the part usually intensified due to a VPPGF) and a favorably located outflow boundary, making it possible to design controlled experiments that focus on these two key structures relevant for tornadogenesis. Note that we are not attempting to explain the formation of an optimal updraft and cold pool, but merely study how changes in these structures influence the development of tornado-like vortices in our simulations.

Altogether, even though the DJB93 mechanism has been shown to be the dominant contributor to at least the initial formation of near-surface vertical vorticity, and it has long been known that the intensification of the low-level updraft is strongly linked to tornadogenesis (e.g., Wicker and Wilhelmson 1995; Trapp et al. 2005), their relative importance remains unclear. Recently, Trapp et al. (2017) also suggested that tornado intensity may be directly related to updraft width per application of Kelvin's circulation theorem. Although additional factors such as surface drag are likely important in real supercells, it is still unclear if, for example, using a semislip bottom boundary condition in supercell simulations is actually less flawed than the simpler free-slip closure (Markowski et al. 2019). Thus, this study focuses on the two main mechanisms that, based on our current understanding, are necessary for the initial stages of tornado formation in supercells (baroclinic generation of vorticity and low-level updraft structure). Specifically, this paper addresses three questions:

1) What is more important for tornadogenesis, the amount of vorticity production within the downdraft, or the strength of the low-level updraft (i.e., if there is a strong updraft but little surface vertical vorticity, is tornadogenesis still possible)?
2) Why can supercells that look very similar on the storm scale behave so differently when it comes to tornado potential?
3) How do differences in vorticity production, low-level updraft strength or updraft width influence the timing and maximum strength of the tornado?

We will investigate these questions by conducting three experiments in which either the low-level updraft strength, the cold pool strength or the updraft width are varied separately, while holding the other ones constant. The remainder of the paper is structured as follows. In section 2, we will introduce details on the model setup including the heat source and sink parameterizations used to mimic a supercell low-level updraft and cold pool. An overview of the experiments will also be given. These experiments will then be presented and discussed in sections 3 and 4, respectively, followed by a summary in section 5.

2. Methods

a. Model setup

We used the Cloud Model 1 (CM1; Bryan and Fritsch 2002), version 19.7, for idealized simulations of a supercell-like low-level updraft and cold pool. Moisture, Coriolis force, surface fluxes, and radiative transfer were not included. The top and bottom boundary conditions were free-slip. The model domain size was 90 km × 90 km in the horizontal and 5 km in the vertical. In the central 20 km × 20 km, the horizontal grid spacing was 100 m, and then increased to 1900 m toward the domain boundaries, using the stretching function in Wilhelmson and Chen (1982). Vertically, the grid was stretched using the same function, from 60 m at the lowest level (30 m AGL) to 140 m at 5 km AGL. The base state temperature profile was adopted from earlier highly idealized simulation studies (Walko 1993; MR14; Houston 2016) with a constant increase in potential temperature up to model top at 5 km (Fig. 1b). As will be explained next, the low-level updraft was directly controlled in the model, making it less sensitive to the wind profile. However, for generation of updraft rotation and better comparability with other studies, we used a standard quarter-circle hodograph with moderate shear (Fig. 1a). To represent a right-moving supercell, the wind profile was shifted so that the expected storm motion (Bunkers et al. 2000) would be approximately stationary.

To conduct controlled experiments on the low-level supercell updraft without actual release of CAPE, we modified the "toy model" approach from MR14, who applied a heat source of cylindrical shape that maintained the storm scale updraft of a supercell. The heat source (S_w) was described as a

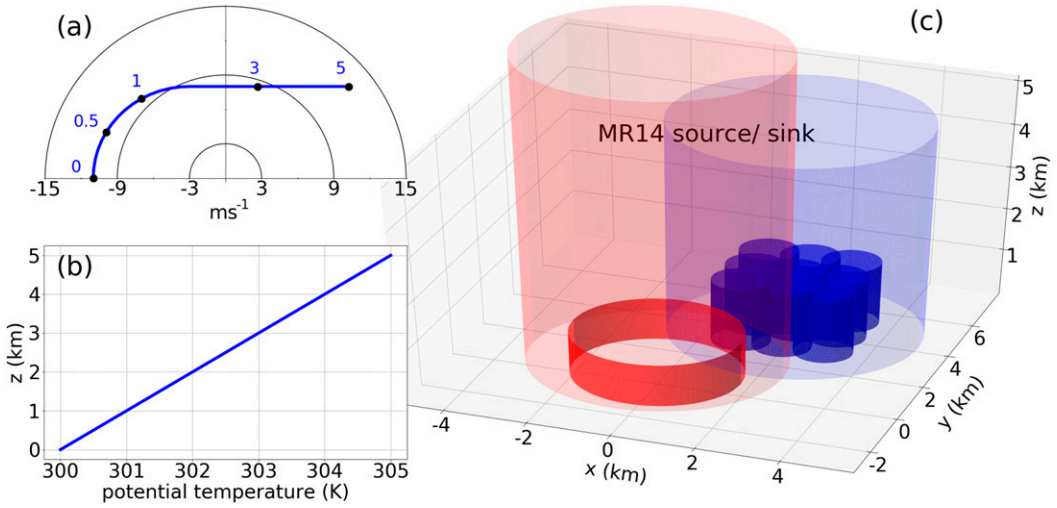

FIG. 1. General model setup with (a) base-state wind profile (selected heights indicated in km), (b) base-state potential temperature profile, and (c) positions of heat source (red) and sinks (blue). The solid cylinders represent the areas where heating or cooling is added to CM1's θ tendency equation in this study while the large transparent cylinders show the setup from MR14 for comparison (since our model top was at 5 km, the MR14 heat source was cut off at $z = 7.5$ km for better visualization).

potential temperature heating tendency that was added to the θ-tendency equation in CM1 as

$$S_w = S_{w0} R(x, y) Z(z), \tag{1}$$

where S_{w0} is the heating magnitude (K s^{-1}) that determines the heat source strength. The functions $R(x, y)$ and $Z(z)$ describe, respectively, the lateral and vertical decreases of the heating rate with distance from the center of the cylinder. In contrast to MR14, the present study aimed to specifically reproduce and control the low-level updraft of a mature supercell by employing a shallower heat source (Fig. 1c). Therefore, the heat source center was fixed at $x = 0$, $y = 0$, and $z = 700$ m AGL, and with a half depth of 500 m the heating was consequently limited to heights between 200 and 1200 m AGL, in contrast to the whole column in MR14. This resulted in an updraft that was most intense between 1 and 4 km AGL (also limited by the domain top at 5 km), much shallower than in other supercell studies (Fig. 2). Details about the setup can be found in Table 1, and the modified CM1 code and namelist files are available in the online supplemental material.

In all model runs, the heat source was started at zero seconds, and the resulting artificial low-level updraft reached a steady, rotating state after a stabilization period of around 900 s. Figure 2 shows that larger S_w values resulted in a stronger low-level updraft. Increasing the radius of the heat source had a similar effect, but also broadened the updraft (not shown). The artificial updrafts in this study were chosen to represent a broad range of potentially tornadic supercells with large vertical velocities (between 7 and 13 m s^{-1} in 500 m AGL) while being compatible with full-physics simulations (e.g., Wicker and Wilhelmson 1995; Orf et al. 2017; Coffer et al. 2017). Furthermore, the tilting of environmental streamwise vorticity resulted in mesocyclonic rotation with realistic values of vertical vorticity (e.g., Skinner et al. 2014). At 900 s into the simulations, artificial cold pool production was started, as explained next.

b. *Achieving realistic cold pools using multiple, time-dependent heat sinks*

Similarly to the heat source parameterization above [Eq. (1)], a negative potential temperature tendency S_c was added to all simulations to reproduce an artificial supercell-like cold pool. Even though the MR14 pseudostorms exhibited some heterogeneity, their single heat sink approach did not fully account for smaller scale downdrafts and the time-dependent structure of real outflow, which is caused by turbulence, microphysical processes and the pulsating character of the updraft. Therefore, different configurations of heat sinks have been tested, resulting in an array of nine small heat sinks (Fig. 1c). The heat sinks S_c were made time dependent by adding periodic fluctuations F_c to Eq. (1) as

$$S_c = \begin{cases} (S_{c0} + F_c) R(x, y) Z(z), & \text{if} \quad t \geq t_{\text{start}} \\ 0, & \text{otherwise}, \end{cases} \tag{2}$$

where $F_c = -(2/3) S_{c0} \cos\{2\pi[(t - t_{\text{start}})/T]\}$ produces an oscillation of the heat sink strength with an amplitude[2] of $(2/3)S_{c0}$. For each of the heat sinks a different activation time (t_{start}) and period of the fluctuations (T) was assigned to produce a chaotic behavior. The activation times were set randomly between 900 and 1050 s and the fluctuation periods between 300 and 500 s (Table 1), aiming for realistic downdraft time scales (e.g., Orf et al. 2012; Gunter and Schroeder 2015). These predefined

[2] Other amplitudes for the oscillations were tested, changing the individual outcomes but not the overall results, so only the $(2/3)S_{c0}$ implementation will be presented here.

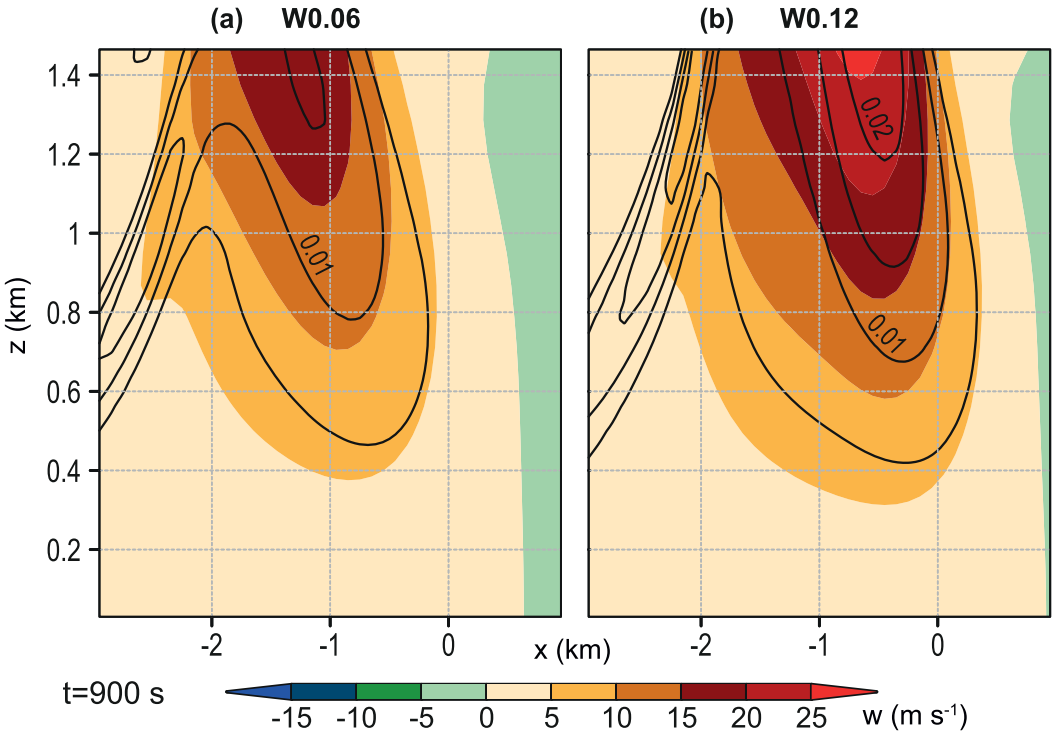

FIG. 2. Cross sections through the low-level updrafts for (a) the weakest and (b) the strongest heat source used in experiment 1 (referred to as W0.06 and W0.12 in the text) with vertical velocity (shaded) and vertical vorticity (black contours at 0.005 and 0.01 s^{-1}). The horizontal radius of the heat sources was 2 km. The cross sections were computed along the x axis at $y = 1.3$ km and at 900 s into the simulation, so before the updraft started interacting with the cold pool.

heat sink timings (Table 1) were used in all simulations to make the cold pools as comparable as possible. As a result of the independent pulsing, a more complex and variable near-ground cold pool structure was produced (Fig. 3a) compared to one constant heat sink (Fig. 3b). Over the two hour simulations, the nine heat sinks interacted with each other, causing stronger and weaker outflow phases. Thus, the near-surface vorticity field featured a complex pattern with vertical vorticity sheets or rivers along internal outflow surges (Fig. 3a), which could then be intensified further, as these features moved into the updraft region.

As can be seen in Fig. 1, the heat sink top was at 1500 m AGL, so it was much shallower than the single MR14 heat sink. This had the effect that the outflow momentum was weaker while the same θ deficits could be achieved. Compared to the MR14 pseudostorms, in which the outflow quickly undercut the updraft when a stronger heat sink was used, the setup here allowed for the formation of a fairly stationary outflow boundary over the whole 2 h simulation time. This was desirable in order to exclude the tornadogenesis failure mode of a surging outflow and solely focus on direct effects of the cold pool strength, such as baroclinic vorticity production.

c. *Experiment design*

The setup described above permits independently changing the low-level updraft or cold pool strengths by simply adjusting the S_{w0} or S_{c0} values. Furthermore, the width of the updraft can

TABLE 1. Values used for the parameterization of each heat source and sink for all model runs (in section 3c; the heat source radius was varied as described there). The x and y coordinates are relative to the domain center.

	Heat source	Sink 1	Sink 2	Sink 3	Sink 4	Sink 5	Sink 6	Sink 7	Sink 8	Sink 9
Center x (m)	0	1000	1000	1000	2000	2000	2000	3000	3000	3000
Center y (m)	0	3000	4000	5000	3000	4000	5000	3000	4000	5000
Center z (m)	700	0	0	0	0	0	0	0	0	0
Horizontal radius (m)	2000	700	700	700	700	700	700	700	700	700
Half depth (m)	500	1500	1500	1500	1500	1500	1500	1500	1500	1500
Activation time t_{start} (s)	—	900	1000	950	1050	990	1030	930	970	1020
Period T (s)	—	380	500	450	300	350	380	400	470	440

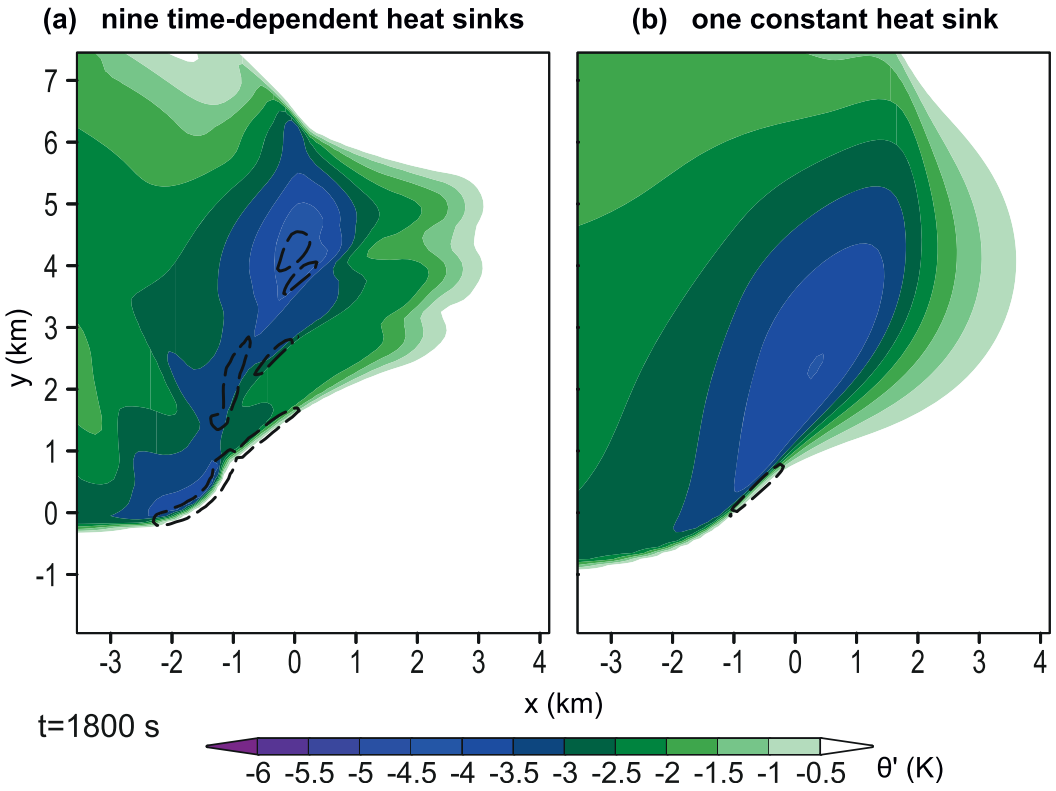

FIG. 3. Cold pool structures at 1800 s in simulations with (a) an array of nine time-dependent heat sinks as used in this study and (b) one time-independent heat-sink. Potential temperature perturbation (θ', shaded) and vertical vorticity (black dashed contour at 0.002 s^{-1}) are shown at 30 m AGL. The simulations used an identical updraft (S_{w0} = 0.08 K s^{-1}) and a heat sink magnitude of (a) S_{c0} = 0.012 K s^{-1} and (b) S_{c0} = 0.008 K s^{-1} and were chosen to reach comparable near-ground θ'.

be changed by prescribing the horizontal radius of the heat source. Upon varying these three parameters separately, this study evaluated three sets of experiments. In the first set of seven model runs (section 3a), different S_{w0} values were implemented to vary the low-level updraft strength, while S_{c0} was held constant (S_{c0} = −0.012 K s^{-1}). These seven simulations will be referred to as W0.06, W0.07, W0.08, W0.09, W0.10, W0.11, and W0.12 in the following, corresponding to the S_{w0} values in these simulations increasing from 0.06 to 0.12 K s^{-1} in 0.01 K s^{-1} increments. For the second experiment (section 3b), a set of 6 simulations (C0.003, C0.006, C0.009, C0.012, C0.015, C0.018) was used to investigate varying the heat sink magnitude S_{c0} from −0.003 to −0.018 K s^{-1} in steps of −0.003 K s^{-1}, while using the same heat source strength (S_{w0} = 0.1 K s^{-1}). These first two experiments in sections 3a and 3b used the same heat source radius of 2000 m. A third experiment in section 3c will evaluate 6 simulations with constant heat source and sink strength but varying heat source radii of 1750, 2000, 2250, 2500, 2750, and 3000 m.

3. Results

a. Experiment 1: Varying the low-level updraft strength

In this section, we will investigate how changes in the low-level updraft strength influenced the development of tornado-like vortices[3] (TLVs) in our pseudostorms. Therefore, the seven simulations to be analyzed (W0.06 to W0.12) were characterized by the same heat sink strength but different heat source strengths. The reader may skip ahead to Fig. 5c to see that a linear increase in the heat source magnitude resulted in linearly changing updraft strengths in these seven simulations, as intended. First, we will look at two example cases (W0.07 and W0.10) and compare how the model fields, especially the near-ground vertical vorticity, evolved over time. Subsequently, a more detailed analysis including parcel trajectories will be presented to explain the observed impact of the low-level updraft strength.

1) GENERAL EVOLUTION OF THE SIMULATIONS

Figure 4 compares the evolution of the near-surface wind and vertical vorticity fields for the W0.07 and W0.10 runs. At 2400 s (Figs. 4a,b), 1500 s after the heat sinks were initialized, both simulations still bore many similarities, because the slight

[3] With surface drag not being included and the grid spacing used, vortices that develop cannot fully represent tornadoes and are merely "tornado-like" vortices. The terms "tornado," "tornadic," and "nontornadic" will refer to these structures when describing the simulations herein.

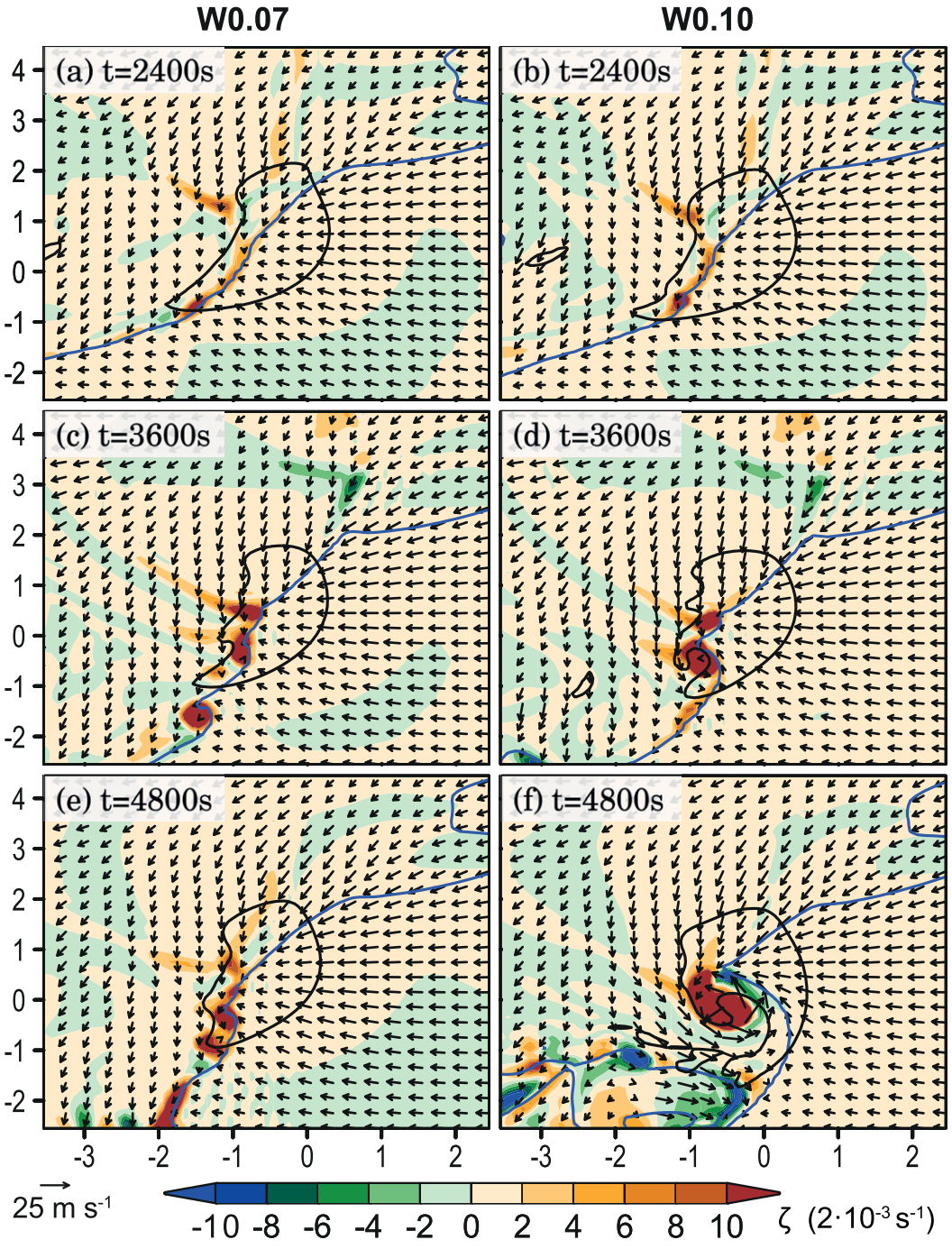

FIG. 4. Evolution of the vertical vorticity field (shaded, 30 m AGL). The nontornadic W0.07 case at (a) 1800, (c) 3600, and (e) 5400 s. (b),(d),(f) The tornadic W0.10 case at the same times as in (a), (c), and (e). The horizontal wind vectors (at 30 m AGL), cold pool extent (-1 K θ', blue contour, 30 m AGL) and outline of the low-level updraft (5 m s^{-1} vertical velocity, black contour, 490 m AGL) are also displayed. The x and y axes represent, respectively, the x and y distances in km.

difference in low-level updraft strength did not influence the overall evolution. At 3600 s (Figs. 4c,d), differences started to become evident in the updraft area, with the W0.10 case developing a closed vortex and a pronounced hook-echo-shaped deformation of the outflow boundary (other areas farther north in the cold pool still showed similar vertical vorticity patches or rivers due to the identical heat sink parameterization). In the following time period, only the W0.10 run showed a

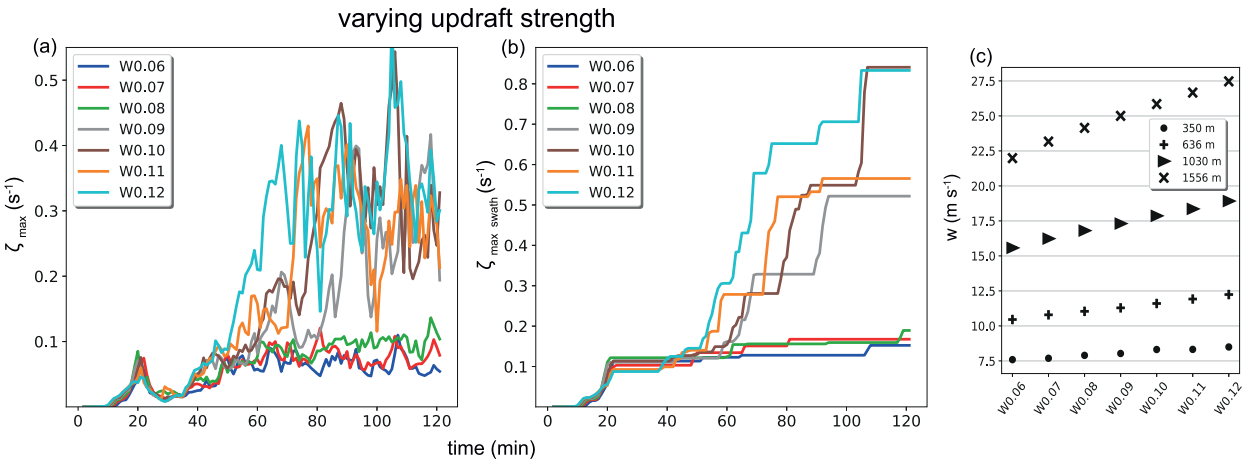

FIG. 5. Vortex and updraft strength for simulations with varying heat source magnitudes. (a) Minute-by-minute maximum vertical vorticity at 30 m AGL. (b) Maximum vorticity swath at 30 m AGL. (c) Horizontal maximum in w at four different heights (averaged between $t = 30$ and $t = 50$ min, i.e., before TLVs were developing).

persistent increase in vertical vorticity until a TLV was established (Fig. 4f). The formation of an occlusion downdraft and a horseshoe-shaped updraft (e.g., Trapp 2002), as well as rear-flank-downdraft (RFD)-like surges, accompanied the rapid increase in near-ground rotation. In contrast, in the W0.07 simulation, smaller vertical vorticity maxima, developing within the outflow, continued to move in and out of the updraft area for the rest of the simulation, without forming a deep TLV (Fig. 4e).

Figures 5a and 5b illustrates this different evolution more generally for all seven simulations. Here, Fig. 5a shows the maximum instantaneous vortex strength in the model output, while Fig. 5b shows the maximum vorticity swath, which is an integrated quantity and therefore includes values in between output times. Three aspects are noteworthy:

- Only the strongest four heat source cases (W0.09 to W0.12) produced a TLV, while the other three runs did not. This means a linear increase in low-level updraft strength did not result in a linear increase in vertical vorticity. Instead, a bifurcation or state transition was evident with two separate regimes, tornadic or nontornadic.
- Among the four tornadic simulations, the stronger the heat source, the earlier and faster a persistent TLV formed ($\Delta t \approx$ 15 min between W0.09 and W0.12).
- A stronger low-level updraft did not necessarily produce a stronger TLV. For instance, the vortex in the W0.10 simulation actually produced the largest near-ground vertical vorticity among all simulations at around $t = 105$ min.

Only in the tornadic simulations did occlusion downdrafts develop and encircle the vorticity maximum. In some of the tornadic runs, the TLVs moved out of the updraft area and decayed. However, in these cases a new TLV formed shortly after, which consistently separated them from the nontornadic runs (Figs. 5a,b). All tornadic simulations frequently exceeded 30 m s^{-1} near-ground horizontal wind speeds, with total maxima of up to 50 m s^{-1} in the strongest cases (not shown).

To explore the robustness of the outcomes, the simulations were repeated with a new random set of activation times and fluctuation periods for the nine heat sinks. As a result, the cold pool character in the simulations changed compared to the simulations presented here. Internal surges were generated at different times, but the overall results remained unchanged, including the separation between nontornadic and tornadic storms in the W0.08 and W0.09 simulations (not shown).[4] In the following section, we will investigate why this bifurcation occurred so consistently.

2) TRAJECTORY ANALYSIS AND THE ROLE OF VORTEX STRETCHING

In our set of simulations, a slight change in updraft strength determined whether near-ground vertical vorticity maxima could be intensified to tornadic strength. Since the expected difference between these cases is the amount of vertical stretching of ζ, which is tied to horizontal convergence via mass continuity, vertical cross sections are shown for the nontornadic case (W0.07) and a tornadic case (W0.10) in Fig. 6 (same cases as shown in Fig. 4). These two cases were not the ones closest to the bifurcation (between W0.08 and W0.09) but were chosen to highlight salient differences between the tornadic and nontornadic cases. The cross sections were taken at the same time and almost perpendicularly to the outflow

[4] Furthermore, simulations were carried out in which the height of the heat source instead of its strength was varied, which resulted in a similar bifurcation. However, we found the height not to be an independent variable, as, for example, increasing the updraft strength influenced the height of a certain vertical velocity level. Therefore, only the impacts of changing the heat source intensity are presented here.

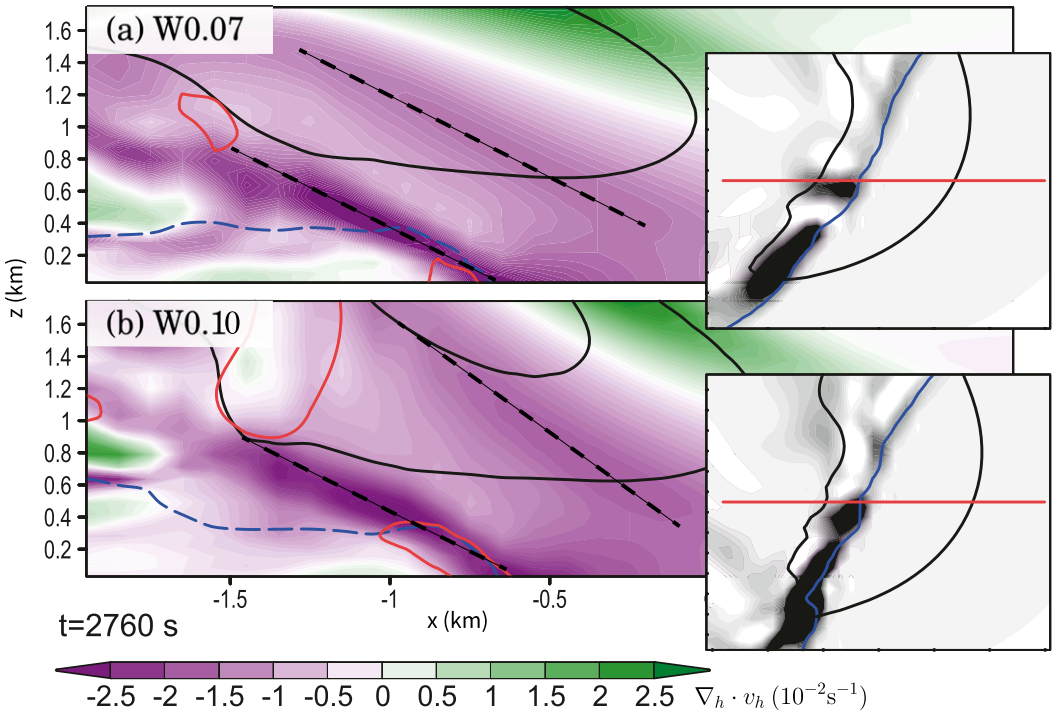

FIG. 6. Vertical cross sections through the cold pool and low-level updraft for the (a) W0.07 and (b) W0.10 simulations. Horizontal divergence (shaded), updraft speed (solid black contours at 10 and 20 m s^{-1}), cold pool extent (−1 K θ', dashed blue contour), and vertical vorticity (red contour at 0.02 s^{-1}) are displayed. Dashed black lines indicate the axes of the two areas with strongest convergence. The side panels show the position of the respective cross section relative to the areas of intensified vertical vorticity (dark shading, 30 m AGL), the updraft area (black contour at 5 m s^{-1} vertical velocity in 490 m AGL), and the −1 K θ' contour at 30 m AGL.

boundary, at the location where the near-ground vertical vorticity was intensifying in each case (Fig. 6). Two separate areas of strong convergence can be seen, one along the outflow boundary and the second below the updraft core. In both simulations, the maximum associated with the gust front was similarly strong and tilted, and it extended from 0 to 800 m AGL. The second maximum, which corresponded to the updraft core, was weaker than the first but extended higher above the outflow boundary and was more erect in the W0.10 simulation. From the opposing outcomes with respect to TLV potential and the knowledge that their only difference lay in the strength of the heat source one would expect major differences in convergence between the two simulations, but the cross sections look surprisingly similar, especially in the lowest kilometer.

To further identify the differences between the simulations, vorticity budgets were calculated along trajectories. One way of finding trajectories would be to identify all parcels that move into an existing TLV and compare them to parcels moving into the strongest vertical vorticity maximum in a nontornadic simulation. However, this approach compares parcels influenced by a tornadic wind and pressure field with those uninfluenced by it. Therefore, since our primary focus was investigating tornadogenesis, we calculated the parcels shortly before tornadogenesis at around 3000 s, when the two simulations still looked similar.[5] As backward trajectories lead to errors in confluent flow (Dahl et al. 2012), a grid of 1.2 million forward trajectories was released at 2100 s (every 100 m horizontally and 50 m vertically). A total of 247 (W0.07) and 272 (W0.10) parcels were found to enter the area with largest vertical vorticity below the updraft at 3000 s. The area was identified subjectively below 300 m AGL (red box in Fig. 7), and a minimum vertical vorticity threshold of 0.001 s^{-1} was used. In both cases the parcels originated between 30 and 500 m AGL and moved directly through the main downdraft, where they descended and took a sharp left turn before reaching their lowest elevation (nadir) at the edge of the updraft area. To obtain a representative vorticity budget, the average parcel was found by syncing all trajectories to reach the nadir at the same reference time. The following filtering criteria were applied to get a realistic average trajectory: 102 (118) parcels were excluded for the W0.07 (W0.1) case because they descended below the lowest

[5] To avoid the relevant trajectories moving out of the center domain with regular grid spacing, the two simulations were repeated with a larger center domain of 30 km × 30 km before the parcels were released. Comparison of the differently gridded simulations showed practically identical model fields in proximity of the updraft.

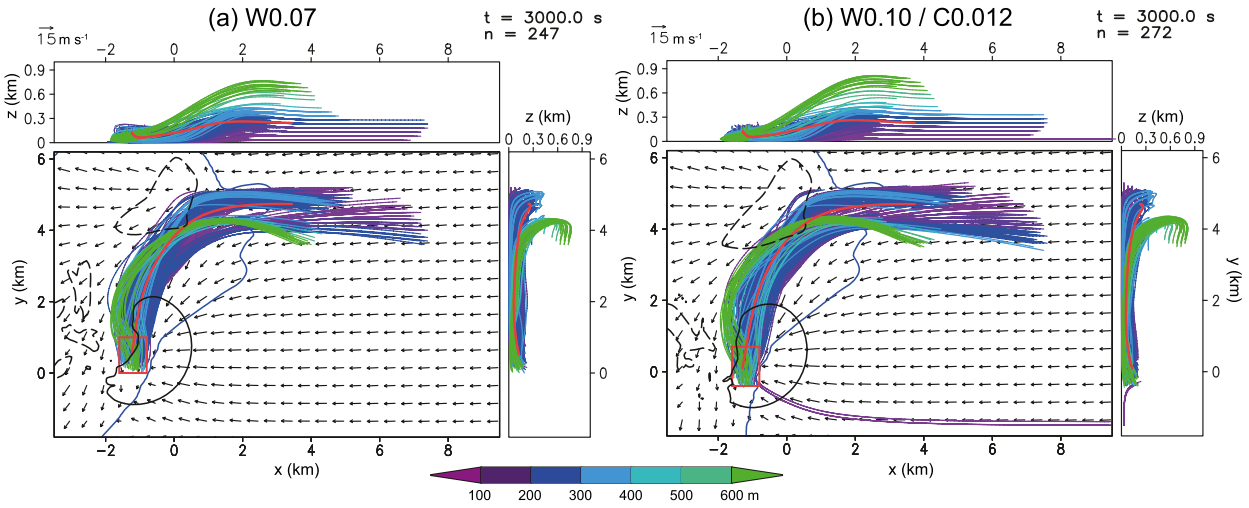

FIG. 7. Forward trajectories of all parcels moving into the area outlined by the red box (below 300 m AGL). (a) The nontornadic W0.07 case and (b) the tornadic W0.10 case. In addition to the color-coded trajectories (warmer colors correspond to increasing height), the horizontal wind vectors (at 30 m AGL), cold pool extent (-1 K θ', blue contour, 30 m AGL), and low-level updraft (5 m s^{-1} vertical velocity, black contour, 490 m AGL) are also shown. The thick red trajectory is the average trajectory of a filtered set of parcels (see text for more information on parcel criteria).

model level (Vande Guchte and Dahl 2018). Out of the remaining dataset, 38 (44) and 31 (46) parcels had to be excluded before averaging since they reached the nadir in the beginning of their trajectory or after 3000 s, leaving 76 (64) parcels for calculation of the vorticity budget of the average parcels whose trajectories can be seen in Fig. 7.

Figure 8 shows the integrated vorticity budgets for the average parcels in the two simulations. Recall that the budgets were calculated prior to tornadogenesis in the W0.10 case to make them comparable, which means that the vertical vorticity only reaches pretornadic values. Starting with the W0.07 case, on average, the magnitude of horizontal vorticity (Fig. 8a) was already nonnegative before the parcels began their descent in the cold pool (at 2200 s), indicating at least some contribution of environmental horizontal vorticity. As the parcels moved over the outflow boundary and entered the area influenced by the heat sinks, the baroclinic term increased and then flattened out, resulting in an average of $|\omega_h| = 0.02\,\mathrm{s}^{-1}$ when the parcels reached the nadir at around 2810 s (tilting and stretching had a minor contribution). Subsequently, $|\omega_h|$ slowly decreased as the parcels started ascending in the updraft area. The z component (ζ) in Fig. 8b was initially zero and fully determined by the tilting and subsequent stretching of the initially horizontal vorticity. It started to become positive as soon as the parcels began their descent and then stayed around $0.005\,\mathrm{s}^{-1}$ until the nadir was reached. Afterward, ζ started to increase further as the parcels moved into the updraft area and contributed to the vertical vorticity maximum of interest at 3000 s (Fig. 7a). For all vorticity components, the integrated terms for subgridscale turbulence and implicit diffusion were negligible. Overall, this budget analysis is consistent with the DJB93 mechanism in the way that horizontal vorticity was produced baroclinically and then reoriented into the vertical while the parcel was still descending.

Moving to the budgets for the W0.10 case in Figs. 8c and 8d, we can see that they are very similar. This was to be expected for the first few hundred seconds of the trajectory since the heat sinks were identical. However, even after the parcels reached the nadir and started ascending, the integrated budgets showed the same development as for the W0.07 run in all vorticity components. Differences in the near-ground vertical vorticity field between the simulations immediately before tornadogenesis can therefore not be explained by differences in storm-scale forcing in the environment of the developing TLV. This suggests a possible feedback mechanism on the scale of the individual vortices, which will be discussed in section 4. Next, we describe the experiments with varying cold pool strength.

b. *Experiment 2: Varying the cold pool strength*

As mentioned in the introduction, some recent studies suggested that the low-level updraft might be more important for tornadogenesis than the production via the DJB93 mechanism. To test this hypothesis, this section will analyze six model runs with different heat sink magnitudes (C0.003, C0.006, C0.009, C0.012, C0.015, C0.018) while using the same strong heat source magnitude ($S_{w0} = 0.1\,\mathrm{K\,s}^{-1}$). Minimum near-surface θ' in the cold pool for the respective simulations were -1, -2.1, -3.2, -4.5, -6.0, and -7.1 K (within 2 km of the typical region of TLV formation or failure). As in experiment 1, the first part of this section will present the general differences between the six simulations. An analysis will follow in the second part.

1) GENERAL EVOLUTION OF THE SIMULATIONS

The overall evolution of the near-ground vertical vorticity field was similar to the experiment before, the difference being that weaker heat sinks produced much weaker initial outflow surges and vortex patches (Fig. 9). However, even with a weaker cold pool, the outflow boundary was still located in a similar position as in the stronger cold pool cases. Inspection of the time series of all six simulations with varying

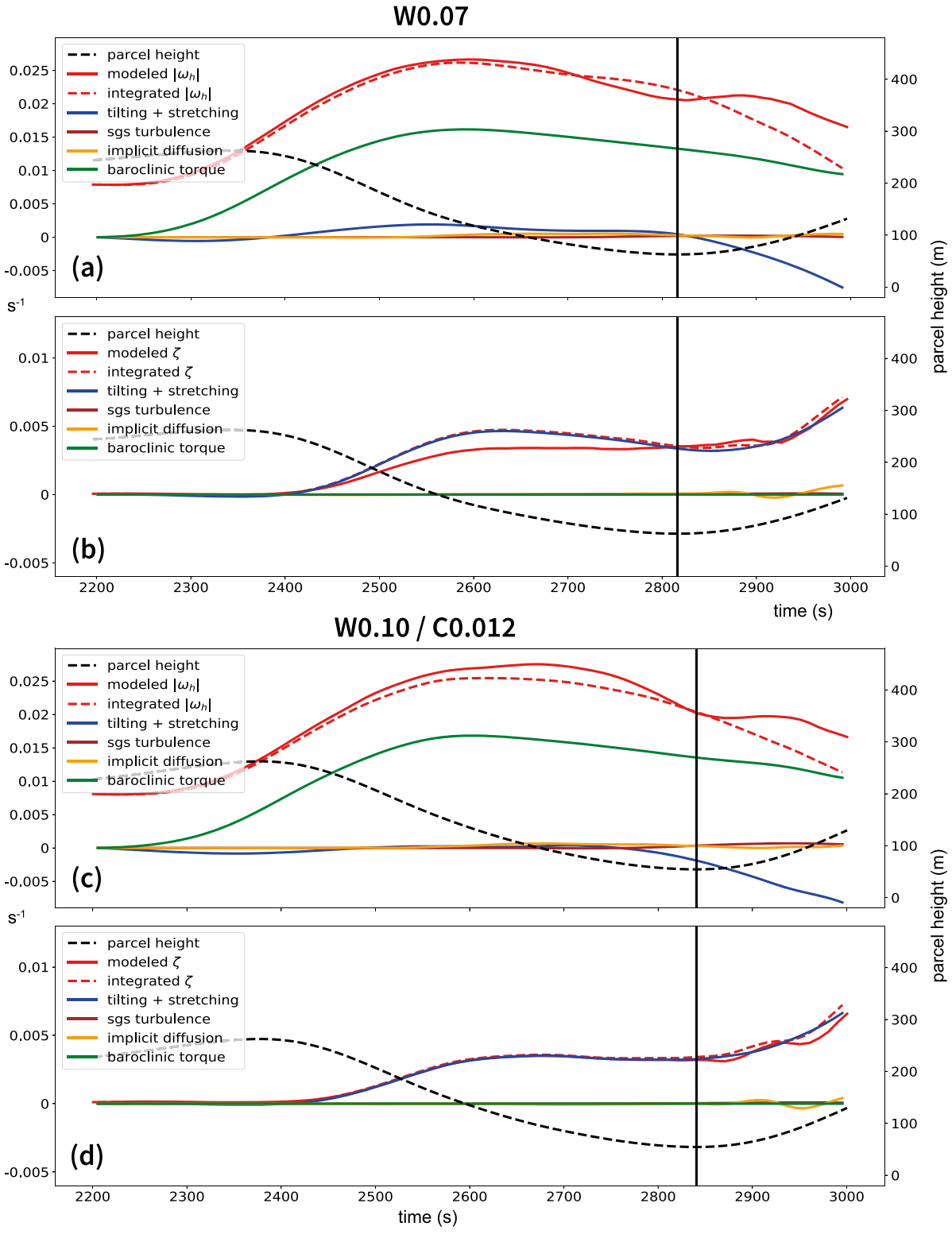

FIG. 8. Integrated vorticity budgets for the average parcel of (a),(b) the nontornadic W0.07 simulation shown in Fig. 7a and (c),(d) the tornadic W0.10 simulation shown in Fig. 7b. The primary y axis gives the amount of vorticity for (a),(c) the horizontal vorticity ($|\omega_h|$) and (b),(d) the z component (ζ). All nonzero integrated terms of the vorticity equation are color-coded following the legend. The dashed red line is the sum of all integrated terms, the solid red line the vorticity value from model output, and the dashed black line the parcel height. The vertical line marks the time of the parcels nadir.

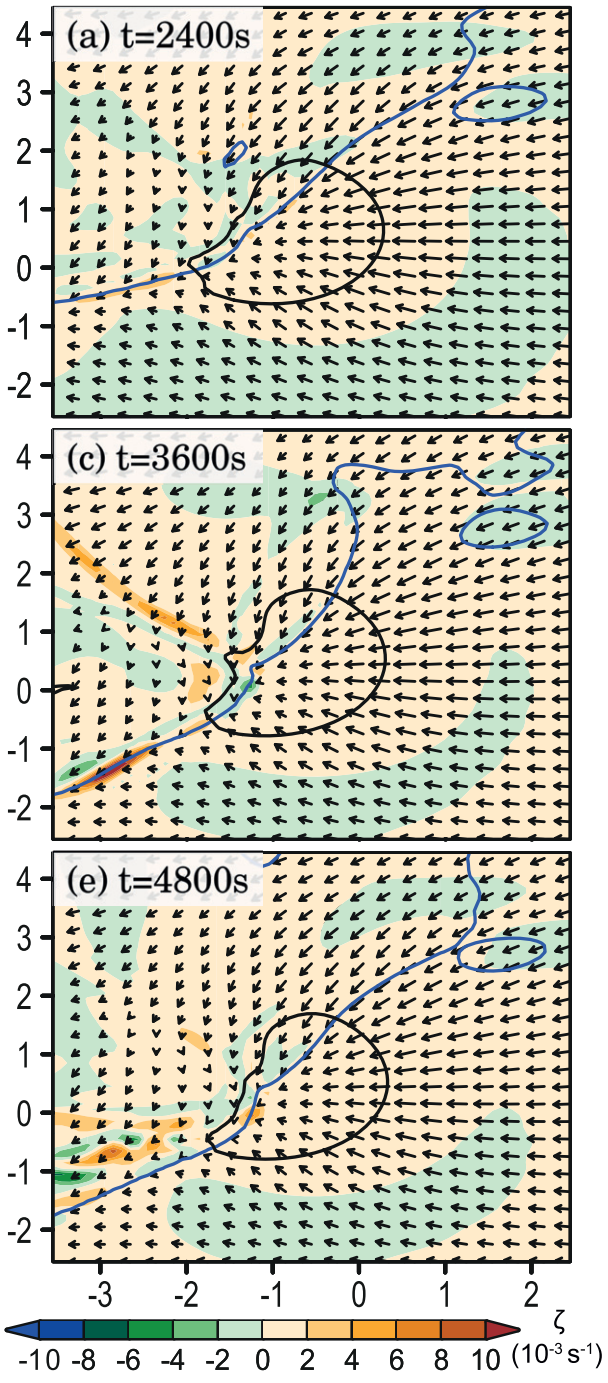

FIG. 9. Evolution of the model fields as in Fig. 4, but for the C0.006 simulation. Note the different scale.

heat sink magnitude (Fig. 10) allows for the following observations:

- A similar bifurcation as in experiment 1 can be seen, with the two weakest heat sink simulations not producing any TLVs. Perhaps surprisingly, these nontornadic simulations did have some vertical vorticity in the right position below the strong low-level updraft (Fig. 9), but it could not be intensified to a TLV.
- The stronger the heat sink, the faster a TLV developed. For instance, it took around 40 min longer in the C0.009 than in the C0.018 simulation to develop a TLV.
- Simulation C0.012 produced the strongest TLV, even though it did not have the strongest cold pool. In addition, a weakening of the updraft was observed at upper levels in the strongest heat sink cases (Fig. 10c) and the tornadic simulations did not reach the peak wind speeds found in the strongest updraft cases of experiment 1 (not shown).

These findings mainly support results of previous studies, defining a range of the cold pool strength that is optimal for tornadoes, also known as ''Goldilocks zone'' (Markowski et al. 2008; MR14). In section 4 we will evaluate this range more precisely for our heat sink magnitudes. However, before that the differences between simulations C0.006 (nontornadic) and C0.012 (tornadic) need to be analyzed further to understand why tornadogenesis failed with the weakest heat sinks, even though a strong updraft was present.

2) TRAJECTORY ANALYSIS AND EFFECTS OF COLD POOL DYNAMICS

Figure 11 shows cross sections through the area of strongest near-surface rotation shortly before the first closed vortex is established in the C0.012 run. As in Fig. 6 in the previous section, two main areas of strong convergence were present, associated with the outflow boundary and updraft core, respectively. In the C0.012 case (Fig. 11b), the outflow boundary penetrated further below the updraft than in the C0.006 run (Fig. 11a). Furthermore, the convergence along the outflow boundary in the C0.012 simulation was at least twice as strong as in the C0.006 run, which can only be a result of the stronger heat sinks because the heat source was the same in both simulations. Therefore, the stronger cold pool led to more convergence along the outflow boundary, offering more stretching of vertical vorticity in the lowest few hundred meters. The impact that outflow characteristics can have on the vertical velocity profile, especially in interaction with an overlying updraft, has recently been noted by Houston (2016, 2017) and Hutson et al. (2019).

To further quantify this development of vertical vorticity, trajectories were calculated for the C0.006 run at the same time and with the same procedure as described in the previous subsection, resulting in 92 parcels initially (Fig. 12). Since simulation C0.012 was identical to W0.10 from experiment 1, the reader is referred to Fig. 7b for comparison. The parcels found to enter the local vorticity maximum in C0.006 almost all originated below 200 m AGL and followed a less curved path than seen in the stronger heat sink cases (Fig. 12). This means that the majority of parcels did not move through the main downdraft region of the already weaker cold pool. The effect can be seen in the vorticity budget for C0.006 (Fig. 13), which has been calculated for a mean of 16 parcels after applying the same filtering criteria as in experiment 1 (the majority of the parcels could not be used because they originated at low altitudes and therefore reached the nadir too early or they descended below the lowest model level). The baroclinic production of $|\omega_h|$ and

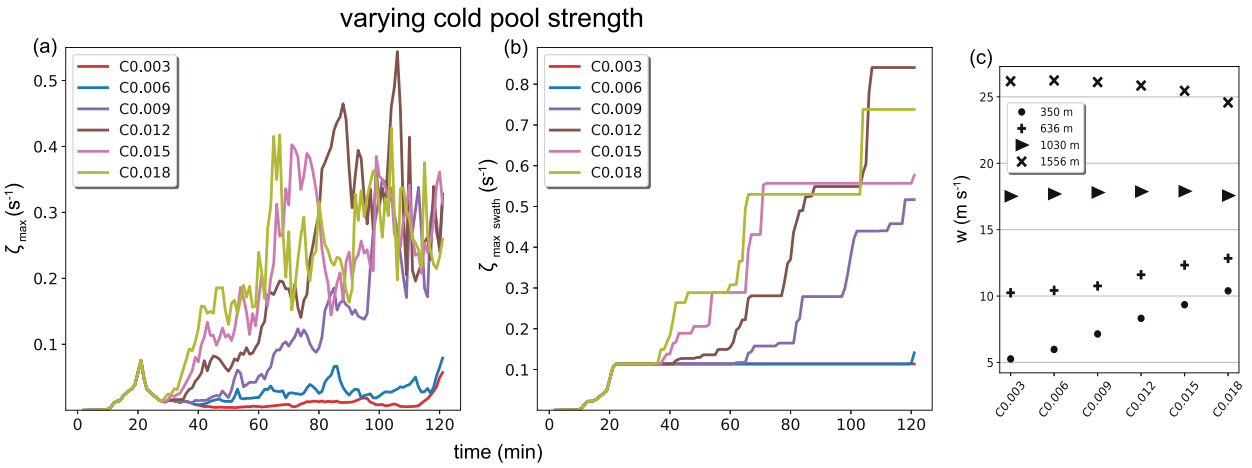

FIG. 10. Maximum vortex and updraft strengths as in Fig. 5, but for the six simulations of experiment 2 (linearly varying heat sink magnitude).

the tilting and stretching of ζ were less than half as large as in the C0.012 simulation (Figs. 8c,d). Consequently, the near-ground vertical vorticity upon entering the updraft area stayed weaker as well.

Overall, these findings suggest that colder outflow enhanced the production of vertical vorticity in this study through multiple factors that are all influenced by the heat sink strength (implying a nonlinear effect on vertical vorticity growth): (i) stronger convergence in the lowest kilometer along the outflow boundary, (ii) a stronger baroclinic torque, (iii) redirection of the parcel trajectories directly through the main downdraft with a longer descent and sharp left turn toward the updraft. It follows, that the weak heat sink cases (e.g., C0.006) stayed nontornadic even though a strong low-level updraft was present, because the weak cold pool limited all the mechanisms above at the same time, greatly reducing the initial vertical vorticity. Thus, in contrast to the experiments varying the updraft strength in the previous subsection, here we do find

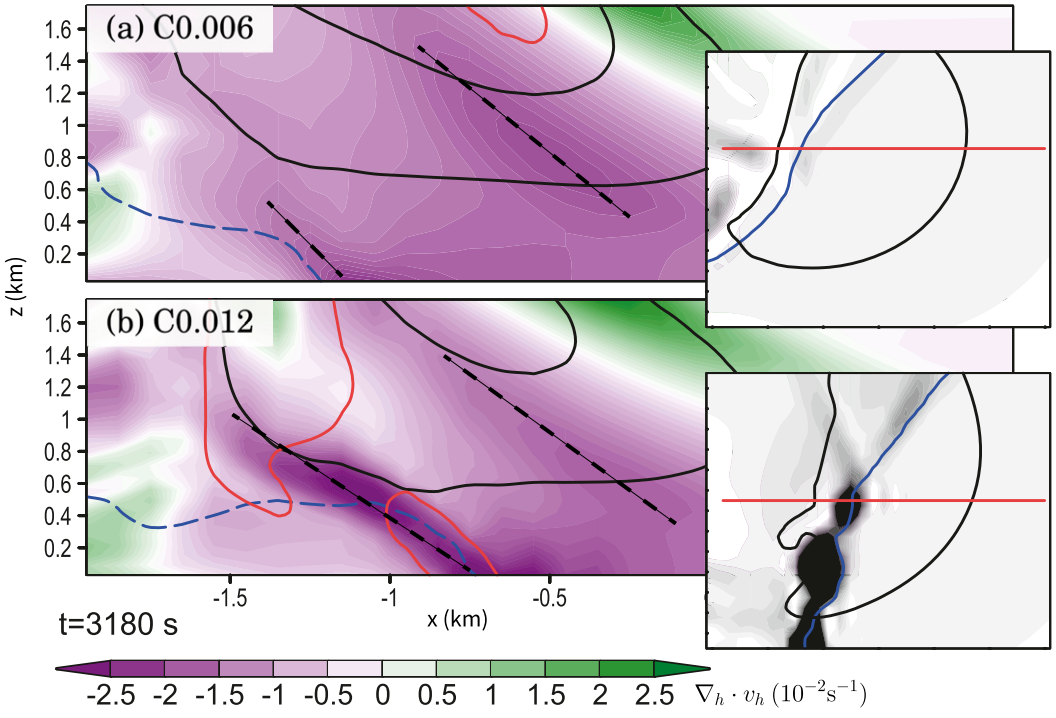

FIG. 11. Vertical cross sections as in Fig. 6, but comparing (a) the C0.006 case with (b) the C0.012 case of experiment 2.

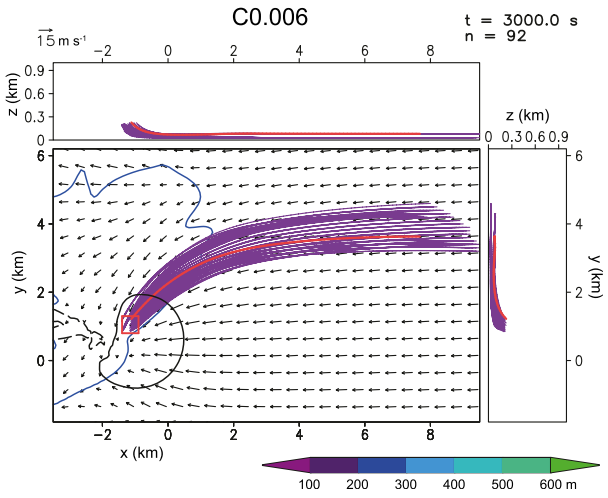

FIG. 12. Trajectories as in Figs. 7a or 7b, but for the nontornadic C0.006 of experiment 2.

differences at the storm-scale that explain at least in part why no TLV develops in C0.006 (a 2 × possible vortex-scale feedback is still possible as discussed in section 4). As a final note, the C0.006 potential temperature deficit was very weak (~1.5 K) compared to typical supercell cases (e.g., Markowski et al. 2002). However, such extreme cases may be realized in LP supercells, in which this small θ deficit in vicinity to the updraft may be realistic.

c. *Experiment 3: Low-level updraft width and vortex strength*

Applying Kelvin's circulation theorem, Trapp et al. (2017) suggested that the width of the mesocyclone could control tornado intensity. We tested this hypothesis in a small set of simulations with different heat source diameters. One of the tornadic runs from our initial dataset with $S_{w0} = 0.12\,\mathrm{K\,s^{-1}}$ and $S_{c0} = 0.012\,\mathrm{K\,s^{-1}}$ was used as control simulation. Recall that the radius of the cylindrical heat source was held constant at 2000 m in all simulations so far. Now the radius was varied in steps of 250 m between 1750 and 3000 m. To hold the updraft strength constant at all levels between these simulations, the S_{w0} value was decreased slightly to compensate for the greater width (Fig. 14b).

In general, the simulations evolved similar to the ones with fixed heat source radius and large S_{w0} and S_{c0} values in the previous subsections. The larger width resulted in stronger inflow and a more pronounced inflow low (not shown). Furthermore, initial intensification of the near-ground rotation happened slightly faster. However, the TLVs that formed in all simulations did not increase in intensity with increasing updraft width. In fact, the maximum vertical vorticity tended to be weaker in the widest and narrowest heat source cases compared to cases with moderate heat source radius (Fig. 14a). The same was true for the maximum near-surface wind speeds (not shown).

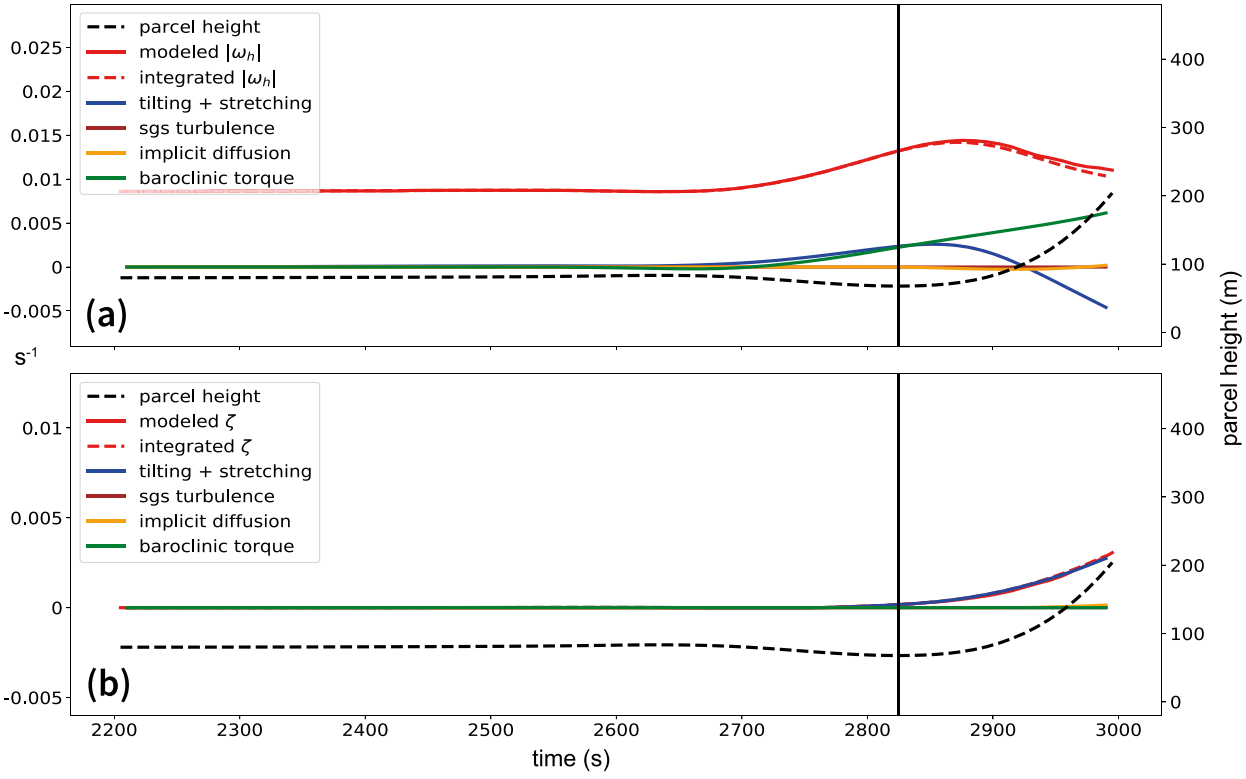

FIG. 13. Vorticity budgets as in Fig. 8, but for the average parcel of the nontornadic C0.006 simulation, which is shown in Fig. 12.

4. Discussion

a. *The relative importance of cold pool and low-level updraft strength*

Experiments 1 and 2 in sections 3a and 3b, respectively, involved the variation of the low-level updraft and cold pool strengths, while holding the other one constant. The same results are highlighted when looking at the whole 2D parameter space of heat source and sink magnitudes, shown in Fig. 15, which represents a set of 88 simulations. Each pixel corresponds to one simulation, performed with the same model configuration as before, which means that experiment 1 is included in column 0.1 K s^{-1} and experiment 2 in row 0.012 K s^{-1}. In addition to the maximum near-ground vertical vorticity in Fig. 15a we also show the time-averaged vertical vorticity at 1030 m AGL in Fig. 15b to specifically consider only vertically coherent TLVs (i.e., supercell tornadoes) compared to shallow vortices that were mostly limited to the lowest levels.

Our general findings are consistent with work by MR14 and others, suggesting that there is a Goldilocks zone most favorable for supercell tornadogenesis and maintenance (e.g., Markowski et al. 2002, 2008). This is demonstrated in the maximum and mean vortex strength per model run in Figs. 15a and 15b, which show optimal TLV potential in a moderate heat sink range.[6] The TLV potential was also increased with greater updraft strength (experiment 1 and Figs. 15a and 15b). Connecting these results, tornadogenesis success or failure was not dominated by one factor alone but instead actively controlled by both the updraft and cold pool strengths (Figs. 15a,b). For example, in experiment 2 it was shown that the vertical vorticity magnitude in the weak cold pool was insufficient to be stretched effectively in the 2 h simulation time, although it ended up in the right position below a strong low-level updraft. Therefore, in addition to MR14, who demonstrated that a weak outflow did not support cyclonic TLVs because of a dislocated outflow boundary, insufficient vertical vorticity in the outflow may also lead to tornadogenesis failure. The question of whether this result is mainly an effect of the decrease in baroclinic vorticity production in the cold pool could not be answered entirely, since other factors that could potentially have an impact on tornadogenesis were sensitive to a varying cold pool strength as well (convergence along the outflow boundary and internal flow structure).

b. *Bifurcation between nontornadic and tornadic cases*

The changes in heat source or sink strength that made the difference between tornadogenesis success or failure were rather small, indicating a bifurcation into two regimes, tornadic or nontornadic. In other words, a linear variation in cold pool or updraft strength did not produce a linear increase in near-surface vertical vorticity. Figures 15a and 15b displays this bifurcation as a large gradient (or jump) in the respective vertical vorticity distribution. Comparison of a nontornadic with a tornadic case having only a slightly stronger updraft revealed that the vorticity budgets of parcels moving into the updraft area prior to tornadogenesis were almost identical (experiment 1). Furthermore, the convergence in the lowest kilometer was maximized along the outflow boundary and therefore similar in both simulations. These findings suggest that stronger low-level updrafts did not simply favor tornadogenesis because of updraft-scale stretching of near-ground vorticity. Instead, there seems to be a mechanism acting on the scale of the individual vortices, forming a closed column of vertical vorticity reaching into the updraft. State transition into a tornadic pseudostorm happened once a certain vortex strength in a vertically coherent column was reached. One might speculate here that the resulting

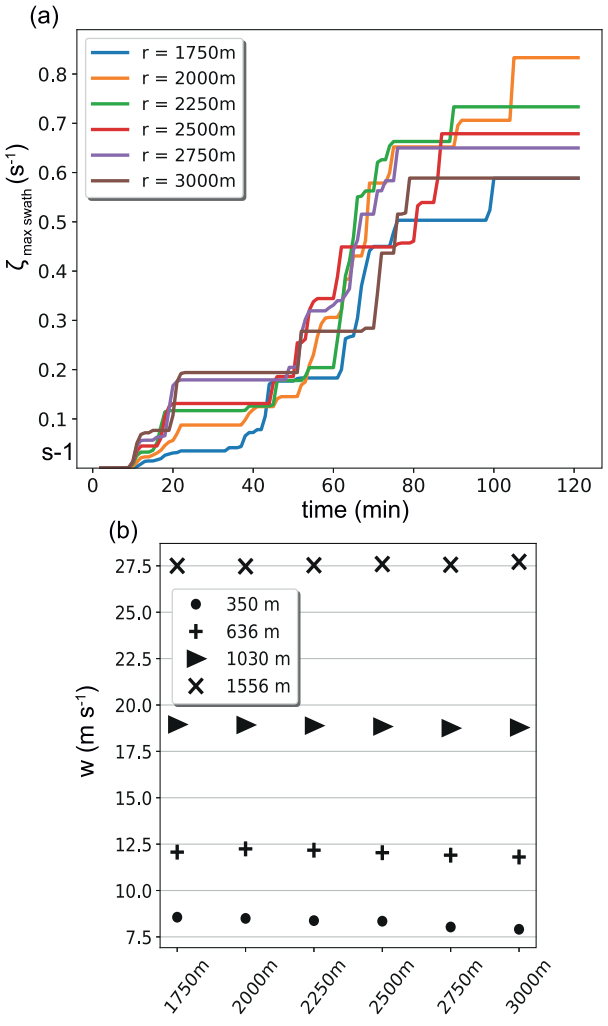

FIG. 14. Maximum vortex and updraft strengths as in Figs. 5b and 5c, but for six simulations with varying heat source radius.

[6] Note that at least short-lived TLVs formed for much lower θ' (see secondary y axis in Fig. 15) than typically observed (e.g., Markowski et al. 2002), because the pseudostorms here were less prone to becoming outflow dominant, and the updraft produced by the strong heat source might have been less vulnerable.

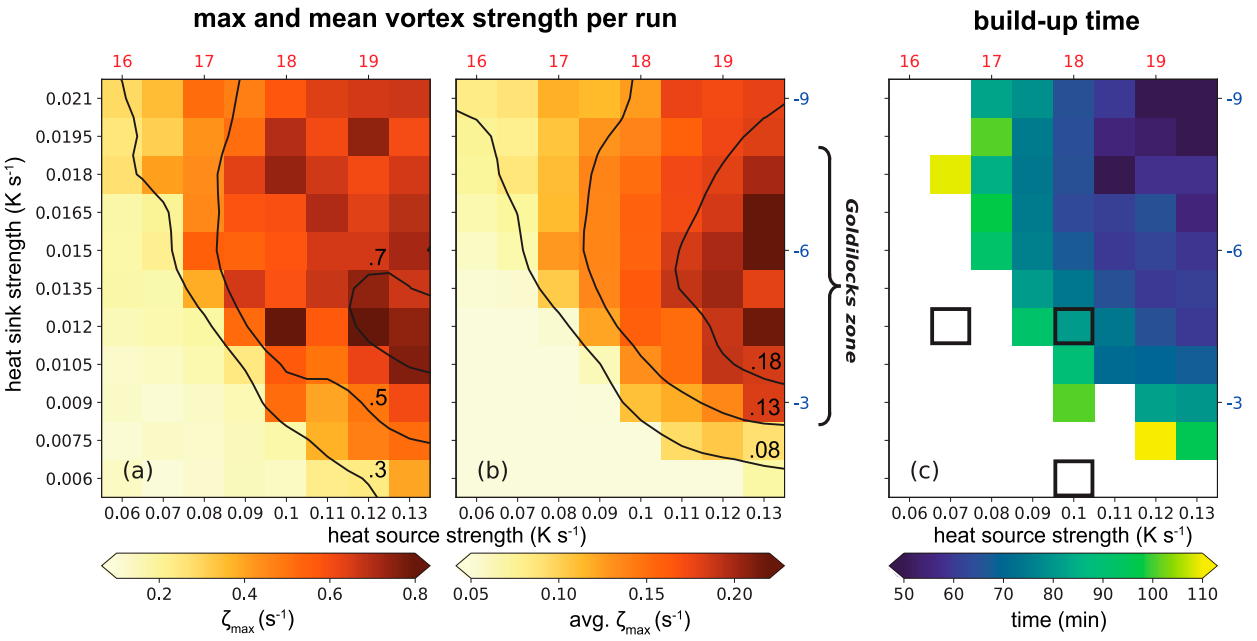

FIG. 15. Vortex characteristics for 88 simulations with different heat source (x axis) and sink (y axis) strengths. (a) Maximum vertical vorticity at the lowest model level (30 m AGL) for each run. The contours were smoothed via a Gaussian filter. (b) Temporal average of minute-by-minute vertical vorticity maxima at 1030 m AGL. (c) Time in minutes at which the 30 m maximum vorticity swath first reached 0.4 s^{-1}. Black boxes indicate the simulations that are analyzed in detail in sections 3a and 3b. For all figures, the secondary x axis shows estimates of the maximum vertical velocity at 1030 m AGL for the given heat source magnitude range (red) and the secondary y axis the average near-surface θ deficits in the cold pool around the updraft area for the heat sink range (blue).

pressure drop in the core (Dahl 2020) could trigger a feedback that is responsible for rapidly increasing vortex strength. Several studies in the past have mentioned the possibility for such a feedback process leading to tornadogenesis (e.g., Lewellen 1993; Wicker and Wilhelmson 1995; Davies-Jones 2008; MR14). An intriguing analogy might be the nucleation of earthquakes, where an initial slip along a fault seems to be required to initiate dynamic rupture (e.g., Scholz 2019). In case of tornadogenesis an initial vorticity magnitude might be needed to provide a sufficiently strong pressure deficit to initiate rapid growth (this feedback seems to involve the pressure deficit and a concomitant increase of tilting of horizontal vorticity as well as stretching of vertical vorticity). The possibility of such a mechanism will be investigated in a future study.

Moreover, the clear separation between tornadic and nontornadic cases, depending on the heat source and sink strengths (Fig. 15), also supports the findings from Coffer et al. (2017), who showed that tornadogenesis success or failure was mostly predetermined by the environment instead of being a stochastic process. At first sight this might appear to contradict the most recent results of Markowski (2020), whose set of 25 ensemble members showed a broad range of tornadic activity from short-lived EF0 to long-lived EF3, despite having almost identical initial conditions. However, all of the ensemble members featured at least one weak tornado, only the intensity and duration were varying drastically. Similarly, in the present study the maximum vertical vorticity did not clearly depend on either the updraft or cold pool strength but was rather randomly distributed across the tornadic cases. This could mean that the possible instability described above and the corresponding changes in the velocity and pressure fields following tornadogenesis may be more important for the maximum TLV intensity than the processes that lead to initial vertical vorticity growth (as long as changes in the updraft or outflow are not extreme or do not lead to TLV decay). The fact that the tornadic simulations showed an increase in updraft strength after tornadogenesis supports this idea. Nevertheless, some impact of the initial updraft strength on existing TLVs was evident here since the average vortex strength in 1030 m AGL consistently increased with heat source magnitude (Fig. 15b).

c. *The aspect of time and possible differences between similar storms*

A final interesting result was the influence of updraft and cold pool strengths on the time it took for the near-ground rotation to intensify until the first TLV formed. This aspect can be clearly seen in Fig. 15c. Differences of up to 60 min could be observed between the optimal and barely tornadic model configurations, respectively. To the authors' knowledge, this relationship has not been discussed in the literature thus far, but it might be important for real supercells for two reasons. First, although many possible outcomes have been documented for merging storms (Lee et al. 2006;

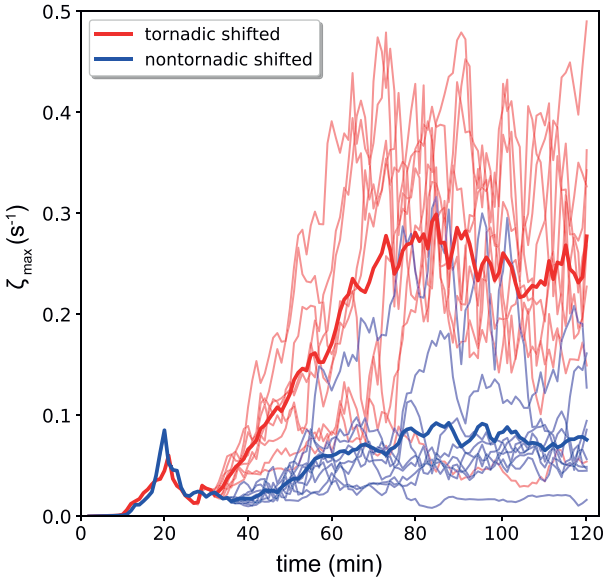

FIG. 16. Hourly vertical vorticity maximum at 30 m AGL for simulations with varied location of the heat sink array relative to the heat source. The red ensemble corresponds to the tornadic test case (S_{w0} = 0.11 and S_{c0} = 0.0135 K s^{-1}) and the blue ensemble to the nontornadic test case (S_{w0} = 0.08 and S_{c0} = 0.009 K s^{-1}). The thick lines in each color show the ensemble mean over the nine simulations.

Hastings and Richardson 2016), the chance that an interaction with another cell (e.g., Klees et al. 2016) or unfavorable changes in the environment interrupt the tornadogenesis process, increases with time. Second, the low-level updraft in real storms is not as steady as modeled here (e.g., Brooks et al. 1993; Coffer and Parker 2018), so overall, the faster a TLV can form, the more likely its genesis will succeed at all. This time aspect might be one reason why visually similar storms differ in their tornadic potential. For example, in a scenario where radar measurements indicate two potentially dangerous supercells and both show intensifying near-surface rotation, only one of the cells might benefit from favorable conditions for tornadogenesis for a long enough time, which would be very difficult to identify. A second reason for the difficulty of distinguishing tornadic and nontornadic supercells may be the bifurcation just discussed. If very slight differences in updraft or cold pool strength can determine if storms become tornadic or not, two virtually identical supercells could be tornadic or nontornadic. These minimal differences would not be observable by currently available platforms. For example, in most cases operational radars can only detect strong low to midlevel rotation, which was present in all of the idealized updrafts used in this study (Fig. 2). Thus, determining which supercell will produce a TLV would have been very difficult, even in this idealized framework without external failure modes.

d. *Sensitivity of the outcomes to the heat sink position and other factors*

We also performed sensitivity tests, which showed that the outcomes illustrated in Fig. 15 (i.e., the location of the bifurcation) were not fixed relative to the given parameter space of heat source and sink strengths, but depended, for example, on the duration of the simulations (some of the nontornadic runs became tornadic after 120 min) or whether a free-slip or semislip bottom boundary condition was used.[7] Therefore, the ranges of updraft and cold pool strengths in this study (for which estimated values of w' and θ' were added as secondary axes in Fig. 15) and the bifurcation zone will likely be different in real storms. However, the key results discussed in the previous subsections should be independent of eventual shifts in the parameter space.

To further explore the possible caveat that the results might change drastically with a different position of the heat sinks relative to the heat source (as found in MR14 and MR17), we performed two more small sets of simulations with varying heat sink position for one tornadic case of the previous dataset (S_{w0} = 0.11 and S_{c0} = 0.0135 K s^{-1}) and one nontornadic case (S_{w0} = 0.08 and S_{c0} = 0.009 K s^{-1}). These cases did not directly lie in the bifurcation region, so some consistency of the TLV potential could be expected. The two ensembles with nine simulations each had the whole heat sink array shifted by ±2 km in the x direction, the y direction, or both, resulting in a regular grid with the initial heat sink location (x = 2, y = 4 km) as center (similar to MR14 who shifted the position by 1 km, resulting in 25 simulations over the same grid). Figure 16 shows that both the tornadic and nontornadic ensemble were relatively robust. Only one of the simulations with strong heat source and sink did not produce a TLV. Its position farthest north of the updraft (x = 0, y = 6 km) is the same as for the Sc8m8 C case in MR17, which they found produced only weak circulation below the updraft. In contrast, only one simulation of the ensemble with weaker heat source and sink produced a TLV with $\zeta > 0.2\,s^{-1}$ (Fig. 16). Interestingly, the position of the heat sink array in this case (x = 0, y = 4 km), was close to the position discussed before, supporting the conclusions from MR14 and MR17 that small differences in the heat sink location can have a big impact on TLV potential. Nevertheless, the TLV potential here appeared to be more consistent than in the studies of MR14 and MR17, which is probably because the comparatively shallow heat sink array lead to a nonsurging outflow boundary that was below the main updraft until the end of the 2 h simulations, allowing for a longer period in which tornadogenesis could succeed.

5. Summary

This study implemented a setup to run controlled experiments on the interaction of a supercell-like low-level updraft and cold pool, parameterized by heat sources and sinks in CM1. A realistic near-ground cold pool structure was achieved by using multiple, time-dependent heat sinks. The simplified pseudostorms successfully produced near-ground supercell

[7] Near-ground vortex structure is less realistic in simulations with a free-slip bottom boundary condition (e.g., Lewellen 1993), but simulations we performed with a semislip condition did behave similarly to their free-slip counterparts.

structures and tornado-like vortices, even though the updrafts in these pseudostorms were limited to heights below the top of the domain at 5 km. This suggests that the mid- and upper-level updraft characteristics of real storms might not play a necessary role in tornadogenesis. Analysis of 88 simulations (Fig. 15) produced the following main findings in light of the three questions posed in section 1:

1) Both the strength of the heat source and heat sink were equally important for tornadogenesis. For instance, even with a strong low-level updraft and the outflow boundary in the right position, tornadogenesis still failed when the cold pool was too weak and did not contain sufficient near-ground vertical vorticity.
2) Very slight changes in either heat source or sink strength determined if the simulation was tornadic or not, indicating a bifurcation between these two regimes. The transition to a tornadic case happened once a vertically coherent column of vertical vorticity with a sufficient pressure drop was established. For supercells in this bifurcation region, accurately forecasting which supercell will produce a tornado might be almost impossible.
3) (i) A stronger updraft or cold pool greatly reduced the time it took for the first tornado-like vortex to form (by up to 60 min, Fig. 15c). In real storms, this aspect might play a crucial role, because favorable conditions, such as a steady low-level updraft, are not given for an unlimited amount of time. (ii) The maximum near-surface vortex strength was not clearly controlled by the updraft strength, updraft width, or cold pool intensity (in this highly idealized setup without influence of surface drag).

Consistent with previous studies, a range of heat sink magnitudes optimal for tornadogenesis was identified in our set of simulations (Goldilocks zone). However, in cases with varying updraft strength, trajectories showed very similar budgets for some of the tornadic and nontornadic runs, indicating that at least in some cases tornadogenesis may depend on vortex-scale feedbacks rather than noticeable storm-scale differences in vorticity production and intensification.

Acknowledgments. We would like to acknowledge George Bryan for providing CM1 and Paul Markowski and Yvette Richardson for the inspiring heat source and sink approach. Furthermore, this work greatly benefited from discussions with Alex Schueth, Brice Coffer, Matt Parker, Adam Houston, Paul Markowski, and Morten Kretschmer over the past year. Yesim Dollar and the three anonymous reviewers are acknowledged for their helpful comments on the manuscript. This work was supported by the National Science Foundation Grant AGS-1651786.

Data availability statement. The CM1 source code and namelist settings are available as online supplemental material.

REFERENCES

Anderson-Frey, A. K., Y. P. Richardson, A. R. Dean, R. L. Thompson, and B. T. Smith, 2016: Investigation of near-storm environments for tornado events and warnings. *Wea. Forecasting*, **31**, 1771–1790, https://doi.org/10.1175/WAF-D-16-0046.1.

Boyer, C. H., and J. M. L. Dahl, 2020: The mechanisms responsible for large near-surface vertical vorticity within simulated supercells and quasi-linear storms. *Mon. Wea. Rev.*, **148**, 4281–4297, https://doi.org/10.1175/MWR-D-20-0082.1.

Brooks, H. E., I. Doswell, A. Charles, and R. Davies-Jones, 1993: Environmental helicity and the maintenance and evolution of low-level mesocyclones. *The Tornado: Its Structure, Dynamics, Prediction, and Hazards, Geophys. Monogr.*, Vol. 79, Amer. Geophys. Union, 97–104, https://doi.org/10.1029/GM079p0097.

Bryan, G., and J. Fritsch, 2002: A benchmark simulation for moist nonhydrostatic numerical models. *Mon. Wea. Rev.*, **130**, 2917–2928, https://doi.org/10.1175/1520-0493(2002)130%3c2917:ABSFMN>2.0.CO;2.

Bunkers, M. J., B. A. Klimowski, J. W. Zeitler, R. L. Thompson, and M. L. Weisman, 2000: Predicting supercell motion using a new hodograph technique. *Wea. Forecasting*, **15**, 61–79, https://doi.org/10.1175/1520-0434(2000)015<0061:PSMUAN>2.0.CO;2.

Coffer, B. E., and M. D. Parker, 2015: Impacts of increasing low-level shear on supercells during the early evening transition. *Mon. Wea. Rev.*, **143**, 1945–1969, https://doi.org/10.1175/MWR-D-14-00328.1.

——, and ——, 2017: Simulated supercells in nontornadic and tornadic VORTEX2 environments. *Mon. Wea. Rev.*, **145**, 149–180, https://doi.org/10.1175/MWR-D-16-0226.1.

——, and ——, 2018: Is there a ''tipping point'' between simulated nontornadic and tornadic supercells in VORTEX2 environments? *Mon. Wea. Rev.*, **146**, 2667–2693, https://doi.org/10.1175/MWR-D-18-0050.1.

——, ——, J. M. L. Dahl, L. J. Wicker, and A. J. Clark, 2017: Volatility of tornadogenesis: An ensemble of simulated nontornadic and tornadic supercells in VORTEX2 environments. *Mon. Wea. Rev.*, **145**, 4605–4625, https://doi.org/10.1175/MWR-D-17-0152.1.

——, ——, R. L. Thompson, B. T. Smith, and R. E. Jewell, 2019: Using near-ground storm relative helicity in supercell tornado forecasting. *Wea. Forecasting*, **34**, 1417–1435, https://doi.org/10.1175/WAF-D-19-0115.1.

Craven, J. P., and H. E. Brooks, 2004: Baseline climatology of sounding derived parameters associated with deep, moist convection. *Natl. Wea. Dig.*, **28**, 13–24.

Dahl, J. M. L., 2017: Tilting of horizontal shear vorticity and the development of updraft rotation in supercell thunderstorms. *J. Atmos. Sci.*, **74**, 2997–3020, https://doi.org/10.1175/JAS-D-17-0091.1.

——, 2020: Near-surface vortex formation in supercells from the perspective of vortex patch dynamics. *Mon. Wea. Rev.*, **148**, 3533–3547, https://doi.org/10.1175/MWR-D-20-0080.1.

——, M. D. Parker, and L. J. Wicker, 2012: Uncertainties in trajectory calculations within near-surface mesocyclones of simulated supercells. *Mon. Wea. Rev.*, **140**, 2959–2966, https://doi.org/10.1175/MWR-D-12-00131.1.

——, ——, and ——, 2014: Imported and storm-generated near-ground vertical vorticity in a simulated supercell. *J. Atmos. Sci.*, **71**, 3027–3051, https://doi.org/10.1175/JAS-D-13-0123.1.

Davies-Jones, R., 1984: Streamwise vorticity: The origin of updraft rotation in supercell storms. *J. Atmos. Sci.*, **41**, 2991–3006, https://doi.org/10.1175/1520-0469(1984)041<2991:SVTOOU>2.0.CO;2.

——, 2008: Can a descending rain curtain in a supercell instigate tornadogenesis barotropically? *J. Atmos. Sci.*, **65**, 2469–2497, https://doi.org/10.1175/2007JAS2516.1.

——, 2015: A review of supercell and tornado dynamics. *Atmos. Res.*, **158-159**, 274–291, https://doi.org/10.1016/j.atmosres.2014.04.007.

——, and H. Brooks, 1993: Mesocyclogenesis from a theoretical perspective. *The Tornado: Its Structure, Dynamics, Prediction, and Hazards, Geophys. Monogr.*, Vol. 79, Amer. Geophys. Union, 105–114, https://doi.org/10.1029/GM079p0105.

Esterheld, J. M., and D. J. Giuliano, 2008: Discriminating between tornadic and non-tornadic supercells: A new hodograph technique. *Electron. J. Severe Storms Meteor.*, **3** (2), http://www.ejssm.org/ojs/index.php/ejssm/issue/view/13.

Gunter, W. S., and J. L. Schroeder, 2015: High-resolution full-scale measurements of thunderstorm outflow winds. *J. Wind Eng. Ind. Aerodyn.*, **138**, 13–26, https://doi.org/10.1016/j.jweia.2014.12.005.

Hastings, R., and Y. Richardson, 2016: Long-term morphological changes in simulated supercells following mergers with nascent supercells in directionally varying shear. *Mon. Wea. Rev.*, **144**, 471–499, https://doi.org/10.1175/MWR-D-15-0193.1.

Houston, A. L., 2016: The sensitivity of deep ascent of cold-pool air to vertical shear and cold-pool buoyancy. *Electron. J. Severe Storms Meteor.*, **11** (3), http://www.ejssm.org/ojs/index.php/ejssm/article/viewArticle/151.

——, 2017: The possible role of density current dynamics in the generation of low-level vertical vorticity in supercells. *J. Atmos. Sci.*, **74**, 3191–3208, https://doi.org/10.1175/JAS-D-16-0227.1.

Hutson, A., C. Weiss, and G. Bryan, 2019: Using the translation speed and vertical structure of gust fronts to infer buoyancy deficits within thunderstorm outflow. *Mon. Wea. Rev.*, **147**, 3575–3594, https://doi.org/10.1175/MWR-D-18-0439.1.

Klees, A. M., Y. P. Richardson, P. M. Markowski, C. Weiss, J. M. Wurman, and K. K. Kosiba, 2016: Comparison of the tornadic and nontornadic supercells intercepted by VORTEX2 on 10 June 2010. *Mon. Wea. Rev.*, **144**, 3201–3231, https://doi.org/10.1175/MWR-D-15-0345.1.

Lee, B. D., B. F. Jewett, and R. B. Wilhelmson, 2006: The 19 April 1996 Illinois tornado outbreak. Part II: Cell mergers and associated tornado incidence. *Wea. Forecasting*, **21**, 449–464, https://doi.org/10.1175/WAF943.1.

Lewellen, W. S., 1993: Tornado vortex theory. *The Tornado: Its Structure, Dynamics, Prediction, and Hazards, Geophys. Monogr.*, Vol. 79, Amer. Geophys. Union, 19–39, https://doi.org/10.1029/GM079p0019.

Markowski, P. M., 2020: What is the intrinsic predictability of tornadic supercell thunderstorms? *Mon. Wea. Rev.*, **148**, 3157–3180, https://doi.org/10.1175/MWR-D-20-0076.1.

——, and Y. P. Richardson, 2014: The influence of environmental low-level shear and cold pools on tornadogenesis: Insights from idealized simulations. *J. Atmos. Sci.*, **71**, 243–275, https://doi.org/10.1175/JAS-D-13-0159.1.

——, J. M. Straka, and E. N. Rasmussen, 2002: Direct surface thermodynamic observations within the rear-flank downdrafts of nontornadic and tornadic supercells. *Mon. Wea. Rev.*, **130**, 1692–1721, https://doi.org/10.1175/1520-0493(2002)130<1692:DSTOWT>2.0.CO;2.

——, C. Hannon, J. Frame, E. Lancaster, A. Pietrycha, R. Edwards, and R. L. Thompson, 2003: Characteristics of vertical wind profiles near supercells obtained from the rapid update cycle. *Wea. Forecasting*, **18**, 1262–1272, https://doi.org/10.1175/1520-0434(2003)018<1262:COVWPN>2.0.CO;2.

——, E. Rasmussen, J. Straka, R. Davies-Jones, Y. Richardson, and R. J. Trapp, 2008: Vortex lines within low-level mesocyclones obtained from pseudo-dual-Doppler radar observations. *Mon. Wea. Rev.*, **136**, 3513–3535, https://doi.org/10.1175/2008MWR2315.1.

——, N. T. Lis, D. D. Turner, T. R. Lee, and M. S. Buban, 2019: Observations of near-surface vertical wind profiles and vertical momentum fluxes from VORTEX-SE 2017: Comparisons to Monin–Obukhov similarity theory. *Mon. Wea. Rev.*, **147**, 3811–3824, https://doi.org/10.1175/MWR-D-19-0091.1.

Orf, L., E. Kantor, and E. Savory, 2012: Simulation of a downburst-producing thunderstorm using a very high-resolution three-dimensional cloud model. *J. Wind Eng. Ind. Aerodyn.*, **104–106**, 547–557, https://doi.org/10.1016/j.jweia.2012.02.020.

——, R. Wilhelmson, B. Lee, C. Finley, and A. Houston, 2017: Evolution of a long-track violent tornado within a simulated supercell. *Bull. Amer. Meteor. Soc.*, **98**, 45–68, https://doi.org/10.1175/BAMS-D-15-00073.1.

Parker, M. D., 2014: Composite VORTEX2 supercell environments from near-storm soundings. *Mon. Wea. Rev.*, **142**, 508–529, https://doi.org/10.1175/MWR-D-13-00167.1.

——, and J. M. L. Dahl, 2015: Production of near-surface vertical vorticity by idealized downdrafts. *Mon. Wea. Rev.*, **143**, 2795–2816, https://doi.org/10.1175/MWR-D-14-00310.1.

Rasmussen, E. N., and D. O. Blanchard, 1998: A baseline climatology of sounding-derived supercell and tornado forecast parameters. *Wea. Forecasting*, **13**, 1148–1164, https://doi.org/10.1175/1520-0434(1998)013<1148:ABCOSD>2.0.CO;2.

Roberts, B., M. Xue, A. D. Schenkman, and D. T. Dawson, 2016: The role of surface drag in tornadogenesis within an idealized supercell simulation. *J. Atmos. Sci.*, **73**, 3371–3395, https://doi.org/10.1175/JAS-D-15-0332.1.

——, ——, and D. T. Dawson, 2020: The effect of surface drag strength on mesocyclone intensification and tornadogenesis in idealized supercell simulations. *J. Atmos. Sci.*, **77**, 1699–1721, https://doi.org/10.1175/JAS-D-19-0109.1.

Rotunno, R., 1981: On the evolution of thunderstorm rotation. *Mon. Wea. Rev.*, **109**, 577–586, https://doi.org/10.1175/1520-0493(1981)109<0577:OTEOTR>2.0.CO;2.

——, and J. B. Klemp, 1985: On the rotation and propagation of simulated supercell thunderstorms. *J. Atmos. Sci.*, **42**, 271–292, https://doi.org/10.1175/1520-0469(1985)042<0271:OTRAPO>2.0.CO;2.

Schenkman, A. D., M. Xue, and M. Hu, 2014: Tornadogenesis in a high-resolution simulation of the 8 May 2003 Oklahoma City supercell. *J. Atmos. Sci.*, **71**, 130–154, https://doi.org/10.1175/JAS-D-13-073.1.

Scholz, C. H., 2019: *The Mechanics of Earthquakes and Faulting*. Cambridge University Press, 512 pp.

Sherburn, K. D., M. D. Parker, J. R. King, and G. M. Lackmann, 2016: Composite environments of severe and nonsevere high-shear, low-CAPE convective events. *Wea. Forecasting*, **31**, 1899–1927, https://doi.org/10.1175/WAF-D-16-0086.1.

Skinner, P. S., C. C. Weiss, M. M. French, H. B. Bluestein, P. M. Markowski, and Y. P. Richardson, 2014: VORTEX2 observations of a low-level mesocyclone with multiple internal rear-flank downdraft momentum surges in the 18 May 2010 Dumas, Texas, supercell. *Mon. Wea. Rev.*, **142**, 2935–2960, https://doi.org/10.1175/MWR-D-13-00240.1.

Thompson, R. L., and R. Edwards, 2000: An overview of environmental conditions and forecast implications of the 3 May 1999 tornado outbreak. *Wea. Forecasting*, **15**, 682–699, https://doi.org/10.1175/1520-0434(2000)015<0682:AOOECA>2.0.CO;2.

——, ——, J. A. Hart, K. L. Elmore, and P. Markowski, 2003: Close proximity soundings within supercell environments obtained from the Rapid Update Cycle. *Wea. Forecasting*, **18**, 1243–1261, https://doi.org/10.1175/1520-0434(2003)018<1243:CPSWSE>2.0.CO;2.

Trapp, R. J., 2002: A clarification of vortex breakdown and tornadogenesis. *Mon. Wea. Rev.*, **128**, 888–895, https://doi.org/10.1175/1520-0493(2000)128<0888:ACOVBA>2.0.CO;2.

——, G. J. Stumpf, and K. L. Manross, 2005: A reassessment of the percentage of tornadic mesocyclones. *Wea. Forecasting*, **20**, 680–687, https://doi.org/10.1175/WAF864.1.

——, G. R. Marion, and S. W. Nesbitt, 2017: The regulation of tornado intensity by updraft width. *J. Atmos. Sci.*, **74**, 4199–4211, https://doi.org/10.1175/JAS-D-16-0331.1.

Vande Guchte, A., and J. M. L. Dahl, 2018: Sensitivities of parcel trajectories beneath the lowest scalar model level of a Lorenz vertical grid. *Mon. Wea. Rev.*, **146**, 1427–1435, https://doi.org/10.1175/MWR-D-17-0190.1.

Walko, R. L., 1993: Tornado spin-up beneath a convective cell: Required basic structure of the near-filed boundary layer winds. *The Tornado: Its Structure, Dynamics, Prediction, and Hazards, Geophys. Monogr.*, Vol. 79, Amer. Geophys. Union, 89–95, https://doi.org/10.1029/GM079p0089.

Wicker, L. J., and R. B. Wilhelmson, 1995: Simulation and analysis of tornado development and decay within a three-dimensional supercell thunderstorm. *J. Atmos. Sci.*, **52**, 2675–2703, https://doi.org/10.1175/1520-0469(1995)052<2675:SAAOTD>2.0.CO;2.

Wilhelmson, R. B., and C.-S. Chen, 1982: A simulation of development of successive cells along a cold outflow boundary. *J. Atmos. Sci.*, **39**, 1466–1483, https://doi.org/10.1175/1520-0469(1982)039<1466:ASOTDO>2.0.CO;2.